

Co-doped Ni hydroxide and oxide nanosheet networks: Laser-Assisted Synthesis, Effective Doping, and Ultrahigh Pseudocapacitor Performance

Dewei Liang^{a,b}, Shouliang Wu^a, Jun Liu^a, Zhenfei Tian^a, Changhao Liang^{a,b,*}

^aKey Laboratory of Materials Physics and Anhui Key Laboratory of Nanomaterials and Nanotechnology, Institute of Solid State Physics, Chinese Academy of Sciences, Hefei 230031, China.

^bDepartment of Materials Science and Engineering, University of Science and Technology of China, Hefei 230026, China.

*Corresponding author. Tel: +86 55165591129; Fax: Tel: +86 55165591434;

E-mail: chliang@issp.ac.cn (C. H. L)

Keywords: doped Ni hydroxide nanosheet, mesoporous structure, laser ablation in liquids, pseudocapacitor performance, synergetic effect

Abstract

Morphology control and impurity doping are two widely applied strategies to improve the electrochemical performance of nanomaterials. Herein, we report an environmentally friendly approach to obtain Co-doped Ni(OH)₂ nanosheet networks using a laser-induced cobalt colloid as a doping precursor followed by an aging treatment in a hybrid medium of nickel ions. The shape and specific surface area of the doped Ni(OH)₂ can be successfully adjusted by changing the concentration of sodium thiosulfate. Furthermore, a Co-doped Ni(OH)₂ nanosheet network was further converted into Co-doped NiO with its pristine morphology retained via facile thermal decomposition in air. The structure and electrochemical performance of the as-prepared samples are investigated with scanning and transmission electron microscopy, energy dispersive x-ray analysis, x-ray diffraction, Fourier transform infrared spectroscopy, the nitrogen adsorption-desorption isotherm technique, and electrochemical measurements. The Co-doped Ni(OH)₂ electrode shows an ultrahigh specific capacitance of 1421 F/g at a current density of 6 A/g, and a good retention level of 76% after 1000 cycles, in sharp contrast with only a 47% retention level of the pure Ni(OH)₂ electrode at the same current density. In addition, the Co-doped NiO electrode exhibits a capacitance of 720 F/g at 6 A/g and 92% retention after 1000 cycles, which is also superior to those values for relevant pure NiO electrodes. The Co²⁺ partially substitutes for Ni²⁺ in the metal hydroxide and oxide, resulting in an increase of free holes in the valence band, and, therefore, enhancement of the *p*-type conductivity of Ni(OH)₂ and NiO. Moreover, such novel mesoporous nanosheet network structures are also able to enlarge the electrode-electrolyte contact area and shorten the path length for ion transport. The synergistic effect of these two results is responsible for the observed ultrahigh pseudocapacitor performance.

1. Introduction

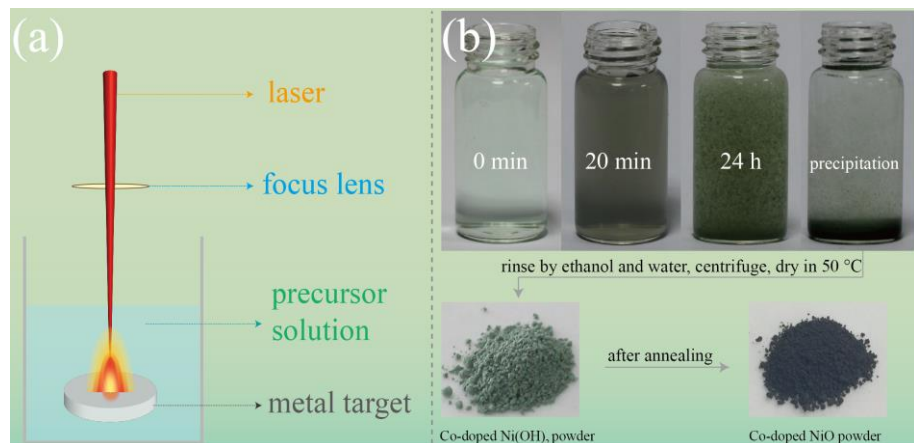
Faced with limited fossil fuel reserves and increasing environmental pollution issues, the demand for clean and renewable energy sources and effective energy storage devices has become increasingly urgent. As a typical energy storage device, supercapacitors have gained considerable attention because of their high power density, fast charge-discharge process, and long cycle lifetime.^{1–5}

Transition-metal oxides and hydroxides with high capacitance capability have been extensively studied for supercapacitor applications. Among transition-metal oxides and hydroxides, Ni(OH)₂ and NiO are considered to be promising active electrode materials for supercapacitors in alkaline electrolytes owing to their layered structure, high theoretical specific capacitance [2358 and 2584 F/g for Ni(OH)₂ and NiO, respectively], lower cost, and natural abundance.^{6–10} Unfortunately, both materials exhibit *p*-type, low electrical conductivity and poor rate capability, which limit their practical electrochemical performance.^{11,12} In order to overcome these intrinsic drawbacks, numerous efforts have been made to improve their electrical conductivity, capacity, rate capability, and reversibility during the charge-discharge processes. One potential approach is to dope them with other elements.^{13–19} The similar size of Ni and Co ion radii make it possible to dope nickel hydroxide-oxide by cobalt without causing serious lattice strain. The Co²⁺ partially substitutes for Ni²⁺ in the metal hydroxide-oxide, which may result in an increase of free holes in the valence band, and, therefore, enhancement of the *p*-type conductivity.^{20–22} Another approach is to increase the specific surface area by construction of a mesoporous structure, which is believed to improve the interface contact efficiency between active sites and electrolytes, to serve as reservoirs for electrolyte ions to facilitate ion and electron transport, and to provide spaces for volume expansion during the cycling process.⁶

Herein, we present a facile and green design to synthesize a Co-doped Ni(OH)₂ interconnected nanosheet network using a laser-induced cobalt colloid as a doping precursor, followed by an aging treatment in a nickel ion and sodium thiosulfate hybrid medium at room temperature (Scheme 1). In

the experiment, laser ablation in liquid (LAL) is a powerful and green technique to generate new nanostructures and nanomaterials without using any stabilizers or surfactants [Scheme 1(a)],^{23–26} and sodium thiosulfate here plays an important role in the reactions as an evocating agent and facilitates the mediation of the shape and specific surface area of the products.²⁷ To the best of our knowledge, this is the first report of a Co-doped Ni(OH)₂ nanosheet network fabricated using the LAL technique for a supercapacitor application. By this method, the as-prepared products possess two merits (doping with Co and formation of a mesoporous structure) in one step. In addition, we also investigate the phase-transition process from Co-doped Ni(OH)₂ to Co-doped NiO with its pristine shape retained, which can be easily realized via thermal decomposition in air [Scheme 1(b)].

The effects of specific surface area and Co doping on pseudocapacitor performance are systematically investigated. It was demonstrated that Co-doped Ni(OH)₂ with large specific surface area displays superior pseudocapacitor performance, shows a higher capacitance of 1421 F/g at 6 A/g, and a good retention level of 76% after 1000 cycles. Also, the Co-doped NiO electrode exhibits a capacitance of 720 F/g at 6 A/g and 92% retention after 1000 cycles. Additionally, both metrics of pseudocapacitor performance are dramatically improved compared to those of undoped components. The synergetic effect of Co-doping and a mesoporous structure is responsible for the observed ultrahigh pseudocapacitor performance.



Scheme 1. (a) Illustration of the LAL technique and (b) photos of precursor and products.

2. Experiment

2.1. Chemicals

All of the chemical reagents used in this study were of analytical grade and used as-received without further purification. Nickel nitrate and sodium thiosulfate were purchased from Aladdin Industrial Corporation (Shanghai, China). Deionized (DI) water was used for all experiments.

2.2. Preparation of a Co-doped Ni(OH)_2 nanosheet network

The nanostructure of a Co-doped Ni(OH)_2 nanosheet network was first synthesized using the LAL technique. In a typical procedure, a cobalt metal plate (99.99% purity) was fixed on a supporter in a vessel filled with 15 mL of mixed solution containing 0.1 M $\text{Na}_2\text{S}_2\text{O}_3$ and 0.02 M $\text{Ni}(\text{NO}_3)_2$. Upon irradiation of the metal plate, the vessel was rotated (10 rpm) by a motorized tunable stage. The metal plate was irradiated using an Nd:YAG pulsed laser at 1064 nm wavelength with an energy density of 130 mJ per pulse and a pulse duration of 10 ns. After irradiation for 20 min, the suspension was stored in a container and aged at room temperature for 24 h. After sufficient growth, the obtained apple-green-colored precipitates were collected and dried in a vacuum at 50 °C overnight (this sample was denoted CN-0.1). For comparison, another sample was synthesized under similar conditions, except that 0.2 M $\text{Na}_2\text{S}_2\text{O}_3$ was used (denoted CN-0.2).

2.3. Preparation of a Co-doped NiO nanosheet network

We selected sample CN-0.1 as the precursor for preparation of the Co-doped NiO nanosheet network because it just needed to be heated in air at 350 °C for 2 h.

2.4. Characterization

The typical morphology and structure of the products were investigated by scanning electron microscopy (SEM, Sirion 200 FEG) and transmission electron microscopy (TEM, JEOL-2010, with

200 kV accelerating voltage). X-ray diffraction (XRD) analysis of the collected powder products was performed by using a Philips X'Pert system with Cu $K\alpha$ radiation ($\lambda=1.5419 \text{ \AA}$). The surface chemical constituents of the products were analyzed by x-ray photoelectron spectroscopy (XPS, Thermo ESCACLB 250). Fourier transform infrared (FTIR) spectra were recorded on a Nicolet 8700 spectrometer by the KBr pellet technique. The surface area and porosity of the samples were measured using an Omnisorp 100CX Analyzer (Beckman Coulter, Inc., USA).

2.5. Electrochemical measurements

Electrochemical measurements were performed on a Zahner electrochemical workstation (IM6) under a three-electrode system at room temperature. The reference and counter electrodes were a Ag/AgCl (saturated KCl) electrode and Pt foil, respectively, whereas the working electrode was prepared by the “drop-casting” method; that is, after polishing and washing the glass carbon electrode (GCE), 5 μL (3 mg/mL) of the as-prepared product dispersion was pipetted onto the treated GCE. After drying the electrode in an ambient environment for 12 h, 10 μL of 5% Nafion[®] solution was added and the sample was dried for another 3 h.

Cyclic voltammetry (CV), electrochemical impedance spectroscopy (EIS), and galvanostatic charge-discharge measurements were conducted in 1 M KOH solution. The CV curves were measured within a 0.1–0.6 V (versus Ag/AgCl) potential window at various scan rates. The EIS measurements of all of the samples were conducted at open-circuit voltage in the frequency range 100 kHz to 0.03 Hz with an alternating current (ac) amplitude of 5 mV. Galvanostatic charge-discharge curves were carried out between 0.1 and 0.55 V. Specific capacitance (C_{SP}) was calculated according to below formula:

$$C_{\text{sp}} = I\Delta t/m\Delta v$$

where C_{SP} (in F/g) is the specific capacitance, I (in A) represents the discharge current, Δv (in V)

represents the total potential deviation, and m (in g) and Δt (in s) are designated the mass of active materials and total discharge time, respectively.

3. Results and discussion

Based on the relevant literature,^{28,29} we have proposed a possible mechanism for the entire formation process of Co-doped Ni hydroxide and oxide nanosheet network structures (Scheme 2); the precursor reactions for the growth of Co-doped Ni(OH)_2 via LAL processes may be expressed as follows:

First, the interaction between the laser beam and cobalt target induces a series of complex physical and chemical processes, which evolve as follows:



The induced ultrafine Co clusters are quasimetastable states possessing large specific surface area and high reactivity,³⁰ which facilitates the doping of Co species into the Ni(OH)_2 crystal lattice. Second, sodium thiosulfate, which plays an important role during the later part of the process, is introduced. On one hand, $\text{S}_2\text{O}_3^{2-}$ ions are adsorbed onto the surface of the as-prepared Co clusters to prevent their growth,³¹ while on the other, $\text{S}_2\text{O}_3^{2-}$ acts as an evocating agent (a soft base) and facilitates the formation of the initial Co-doped Ni(OH)_2 nanosheets.^{32,33}

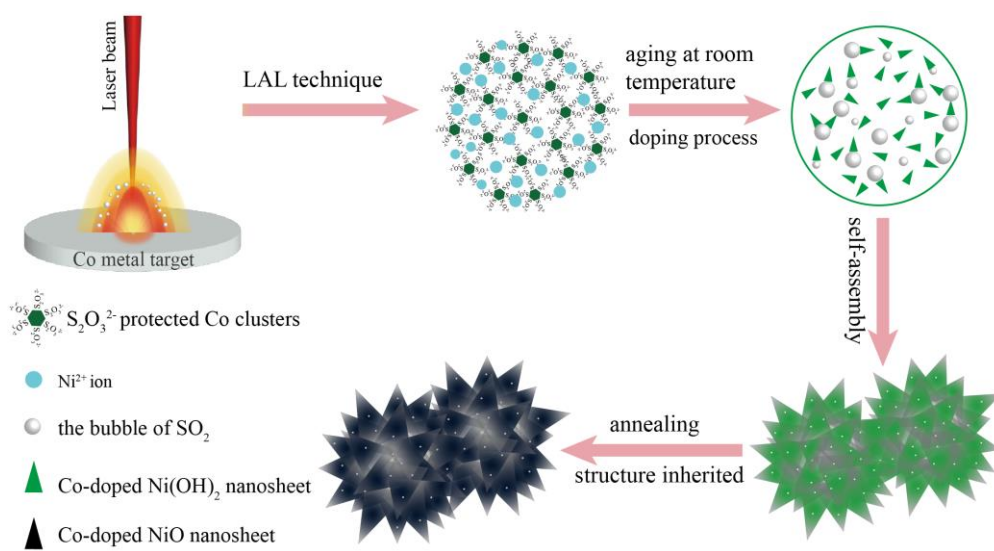


Moreover, $\text{Na}_2\text{S}_2\text{O}_3$ has poor thermal stability and tends to decompose into Na_2SO_4 under laser-induced high-temperature plasma heating. Importantly, the obtained SO_4^{2-} anion can embed into the interlayer of the $\alpha\text{-Ni(OH)}_2$, thus expanding the layer spacing, promoting ion and electron transport,

and providing more spaces for volume expansion during the cycling process.^{34,35}



Third, as the tiny Co-doped Ni(OH)₂ nanosheets continue to grow, the SO₂ bubbles act as soft templates and facilitate the self-assembly of the nanosheets into a network architecture. The formation of mesoporous structures in the nanosheet network is mainly due to the rapid elimination of the excess SO₂ bubbles. Finally, through a simple annealing treatment, we obtain the mesoporous Co-doped NiO nanosheet network.



Scheme 2. Proposed formation process of Co-doped nickel hydroxide and oxide nanosheet network structures.

The phase and composition of Co-doped Ni(OH)₂ samples are then examined by x-ray diffraction (XRD) as presented in Fig. 1(a). The diffraction peaks of the two samples can be assigned to α -Ni(OH)₂ (JCPDS 38-0715), consistent with our previous work.²⁹ No obvious peaks for cobalt oxides, hydroxides, or other impurities are detected, implying that cobalt is successfully doped into the crystal lattice of the α -Ni(OH)₂. Worth noting is that the intensities of the peaks are very weak and broad, which implies the low crystallinity of the flowerlike nanosheets and the small crystalline size of the particles. The synergistic effect of Co doping and low crystallinity leads to the random orientation and

stacking of the layers along the c axis, and results in the absence of (003) and (006) planes. The introduction of sodium thiosulfate resulting in an amorphous structure can be found in previous reports.^{27,32,33} In order to further confirm this specific phenomenon, the nickel metal target was also ablated only in 0.2 M Na₂S₂O₃ solution using the LAL technique, stored in a container, and aged at room temperature for 1 week. The results showed that amorphous Ni(OH)₂ with similar nanosheet-like morphology was successfully obtained (Fig. S1 and S2), which was selected as our subsequent counterpart for comparing the pseudocapacitor performance.

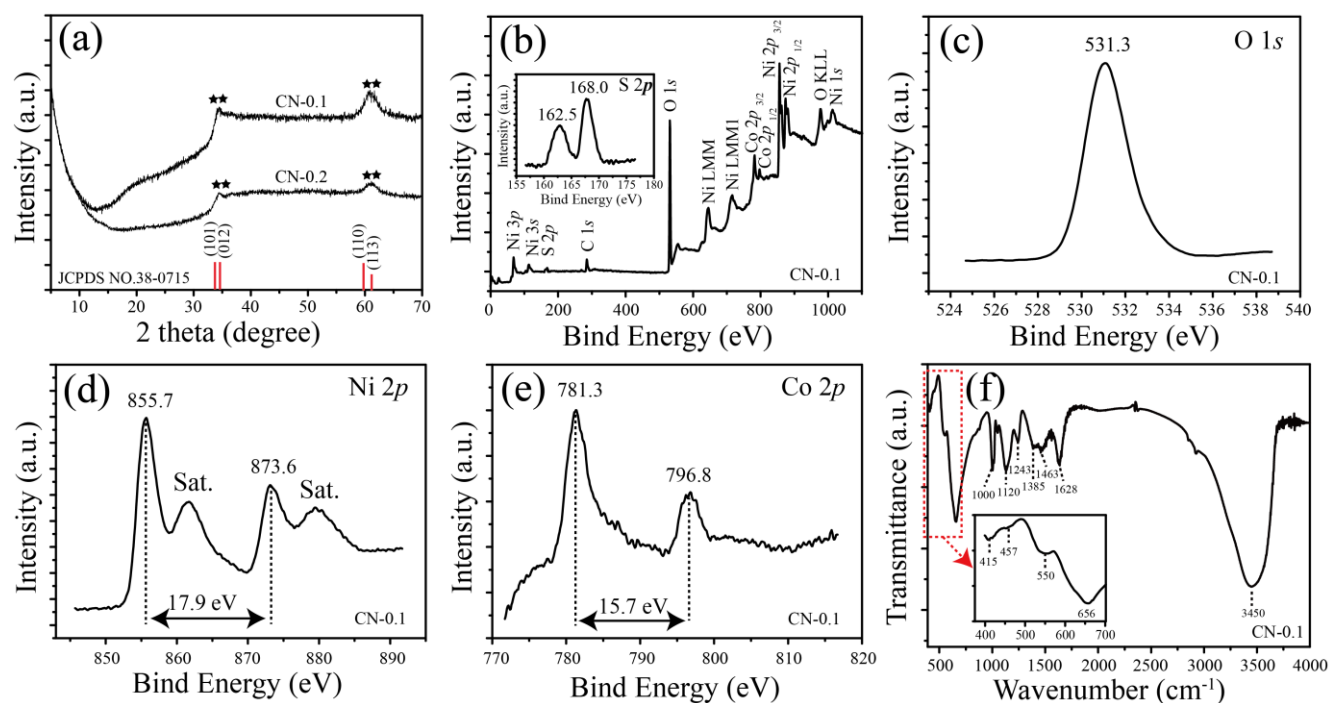


Fig. 1. (a) XRD spectra of samples CN-0.1 and CN-0.2; (b) Survey XPS spectrum for sample CN-0.1, and high-resolution spectra of (c) O 1s, (d) Ni 2p and (e) Co 2p; (f) FTIR spectra of sample CN-0.1.

X-ray photoelectron spectroscopy (XPS) is used to estimate the various chemical states of bonded elements. The survey XPS spectrum for sample CN-0.1 is shown in Fig. 1(b), indicating the presence of Ni, Co, O, and S. According to the *Handbook of X-ray Photoelectron Spectroscopy*, the S peak [inset of Fig. 1(b)] can be associated with the S 2p peak from the intercalated SO₄²⁻ group between the Ni(OH)₂ layers or the absorbed S₂O₃²⁻ on the surface, and the binding energy of 531.3 eV for the O 1s

peak can be mainly derived from a hydroxyl group (O-H) with a binding energy of ~531 eV [Fig. 1(c)]. Figure 1(d) shows the high-resolution Ni $2p_{3/2}$ and Ni $2p_{1/2}$ peaks centered at 855.7 and 873.6 eV, respectively, with a spin-energy separation of 17.9 eV, which is in good agreement with reported data for Ni²⁺.³⁶ In Fig. 1(e), the Co $2p$ XPS spectrum of the sample exhibits two peaks, at 781.3 and 796.8 eV, corresponding to the characteristic Co $2p_{3/2}$ and Co $2p_{1/2}$ peaks, with a spin-energy separation of 15.7 eV, demonstrating the presence of Co²⁺.^{37,38}

In order to further confirm the XRD and XPS results, FTIR is used to characterize sample CN-0.1, as shown in Fig. 1(f). The broad band at 3450 cm⁻¹ is assigned to the O-H stretching vibrations of the interlayer water molecules and hydrogen atoms bound to OH⁻ groups, and the peak around 1628 cm⁻¹ corresponds to the bending vibration of water molecules.^{39,40} The bands at around 656 and 415 cm⁻¹ can be assigned to Ni-O stretching vibrations and an in-plane Ni-O-H bending vibration, respectively,^{41,42} while the bands at around 550 and 457 cm⁻¹ are caused by Co-OH bending and Co-O stretching vibrations.⁴³ Three absorption bands located at 1000, 1385, and 1463 cm⁻¹ are attributed to the characteristic absorption peaks of carbonate ions. The strong absorption peak around 1120 and 1243 cm⁻¹ corresponds to the characteristic peaks of sulphate intercalated between the Ni(OH)₂ interlayers or the absorbed S₂O₃²⁻ on the surface.^{35,44-46}

We investigate the effect of the concentration of sodium thiosulfate on the morphology of the products. Figure 2(a) presents a SEM image of sample CN-0.1. Clearly, the as-prepared samples are composed of many well-defined aggregates with flowerlike morphology approximately 100 nm in size, and they are mutually interconnected to form a network structure, which is beneficial to the electrical conductivity of the bulk. Figure 2(b) shows the interior structure of sample CN-0.1, and proves that the flowerlike aggregates consist of many interconnected nanosheets with a curly shape, endowing the materials with abundant nanocavities and channels. Such a structure with a high percentage of nanocavities, plentiful channels, and mesopores may facilitate the penetration of electrolyte, reduce the

contact resistance, and enhance the mass and charge transfer at the interface of the electrode and electrolyte. The energy-dispersive x-ray spectroscopic (EDS) elemental maps shown in Fig. 2(c) clearly reveal that Co, Ni, and O are homogeneously distributed in the entire nanosheet network.

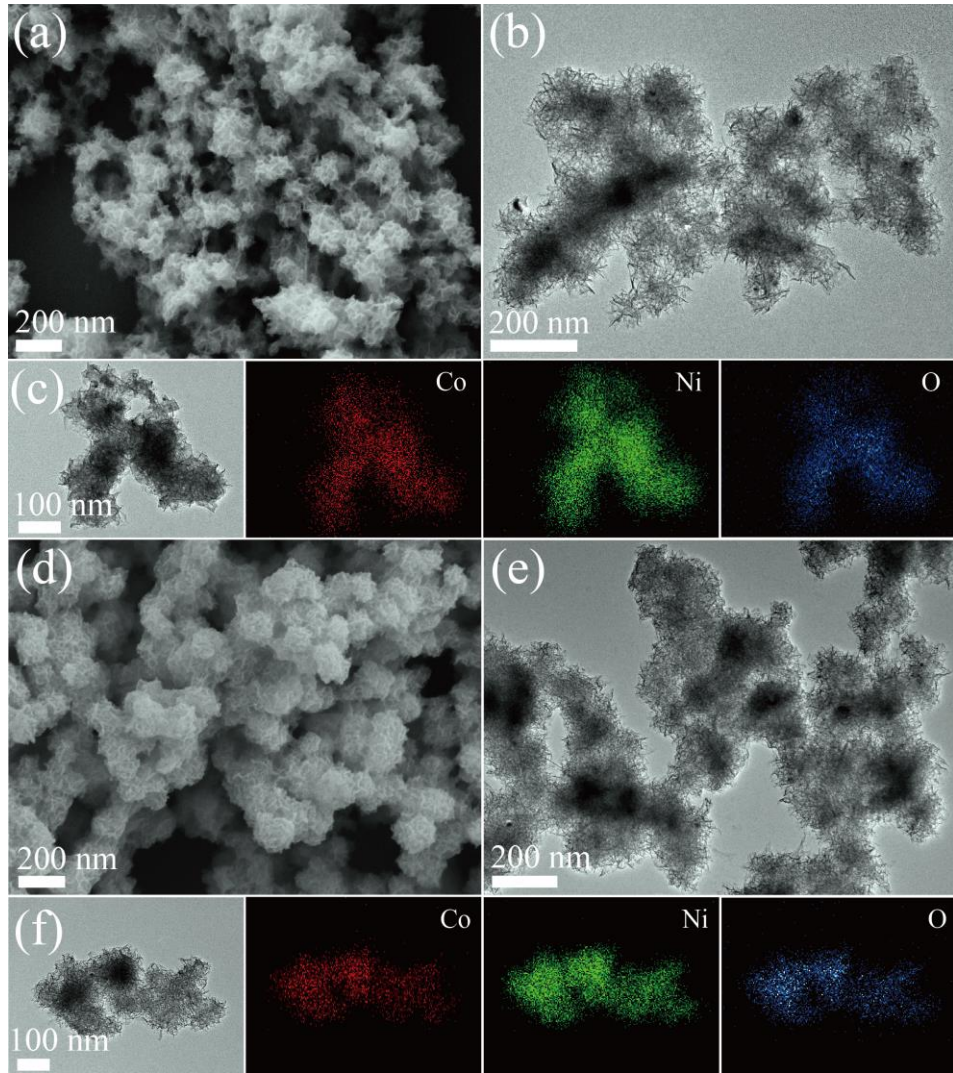


Fig. 2. (a) Field-emission SEM (FESEM) image, (b) TEM image, and (c) corresponding EDS mapping of Co-doped Ni(OH)₂ aggregates synthesized in a 0.1 M Na₂S₂O₃ and 0.02 M Ni(NO₃)₂ mixed solution (CN-0.1); (d) FESEM image, (e) TEM image, and (f) corresponding EDS mapping of Co-doped Ni(OH)₂ synthesized in a 0.2 M Na₂S₂O₃ and 0.02 M Ni(NO₃)₂ mixed solution (CN-0.2).

Figure 2(d) shows a SEM image of sample CN-0.2. After doubling the concentration of sodium thiosulfate, we find that the flowerlike aggregates remain mutually interconnected to form a network

structure, and the morphology of the aggregate becomes more uniform. Figure 2(e) shows the interior structures of aggregates that still consist of many interconnected nanosheets with curly morphology. Co, Ni, and O are homogeneously distributed in the entire nanosheet network as shown in Fig. 2(f).

In order to obtain precise information on specific surface area, nitrogen adsorption-desorption isotherms are performed and are shown in Fig. 3. A small step of nitrogen adsorption and desorption branching occurs, indicating the existence of mesopores in both of the two samples.⁴⁷ The BET surface area of sample CN-0.1 is calculated to be $270.7 \text{ m}^2/\text{g}$ [Fig. 3(a)]. After doubling the concentration of sodium thiosulfate, the BET surface area [Fig. 3(b)] decreases to $162.4 \text{ m}^2/\text{g}$. The pore diameter distribution data are obtained from the Barrett-Joyner-Halenda (BJH) model, and the result shows that both samples have a similar pore diameter distribution around 3.8 nm. The large surface area and abundant mesopores can facilitate exposure of active sites and mass transportation, which is expected to have a good effect on the improvement of the electrochemical properties as supercapacitor.

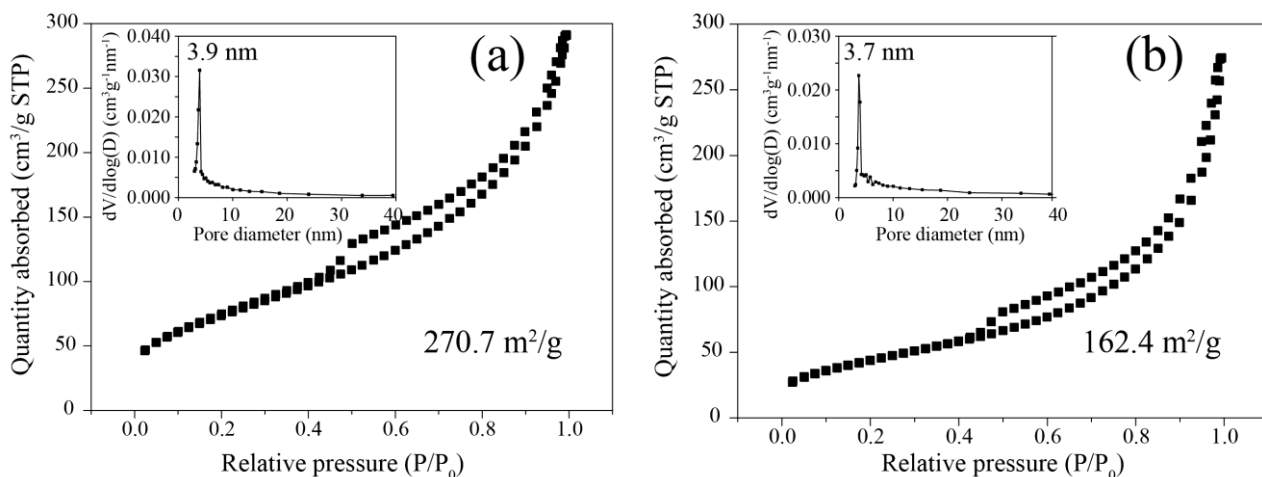


Fig. 3. Typical N_2 adsorption-desorption isotherms and pore-size-distribution curves (inset) of samples (a) CN-0.1 and (b) CN-0.2.

The electrochemical performance of these two samples as electrode materials for supercapacitors is characterized by cyclic voltammetry and galvanostatic charge-discharge measurements in 1 M KOH. Figure 4(a) presents a comparison of the CV curves of samples CN-0.1 and CN-0.2 at a scan rate of 10

mV/s. Two strong redox peaks are observed for the two sample electrodes, indicating the pseudocapacitive performance of the supercapacitor. The anodic and cathodic peaks are attributed to the conversion between $\alpha\text{-Ni(OH)}_2$ and $\gamma\text{-NiOOH}$ due to OH^- insertion and desorption.^{8,46} The reactions involved are illustrated as follows:



Moreover, the integral area of CN-0.1 is higher than that of CN-0.2, indicating a higher specific capacitance. Figures 4(b) and 4(c) present the CV curves of CN-0.1 and CN-0.2 measured at scan rates from 5 to 50 mV/s. Clearly, the oxidation peak shifts in the positive direction and the reduction peak shifts in the negative direction with the increase of the scan rate, which is mainly due to the internal resistance of the electrode.⁴⁸ To further qualify the specific capacitance of the products, a chronopotentiometry test is carried out at various current densities, and the typical discharge curves are depicted in Figs. 4(d) and 4(e). The nonlinear discharge curves demonstrate that typical Faradaic redox reactions occur at the electrode-electrolyte interfaces, reconfirming their typical pseudocapacitive characteristic.⁴⁹ The specific capacitances calculated from the discharge curves are plotted in Fig. 4(f), which shows both gradually decreasing with increasing current density. Specifically, the CN-0.1 electrode exhibits high specific capacitances of 1421, 1333, 1233, and 1156 F/g at current densities of 6, 10, 15, and 20 A/g, respectively, and ~82% of the specific capacitance is still maintained when the charge-discharge rate increases from 6 to 20 A/g. In contrast, the CN-0.2 electrode exhibits specific capacitances of 1093, 956, 900, and 844 F/g at the same current densities, and ~77% of the specific capacitance is maintained.

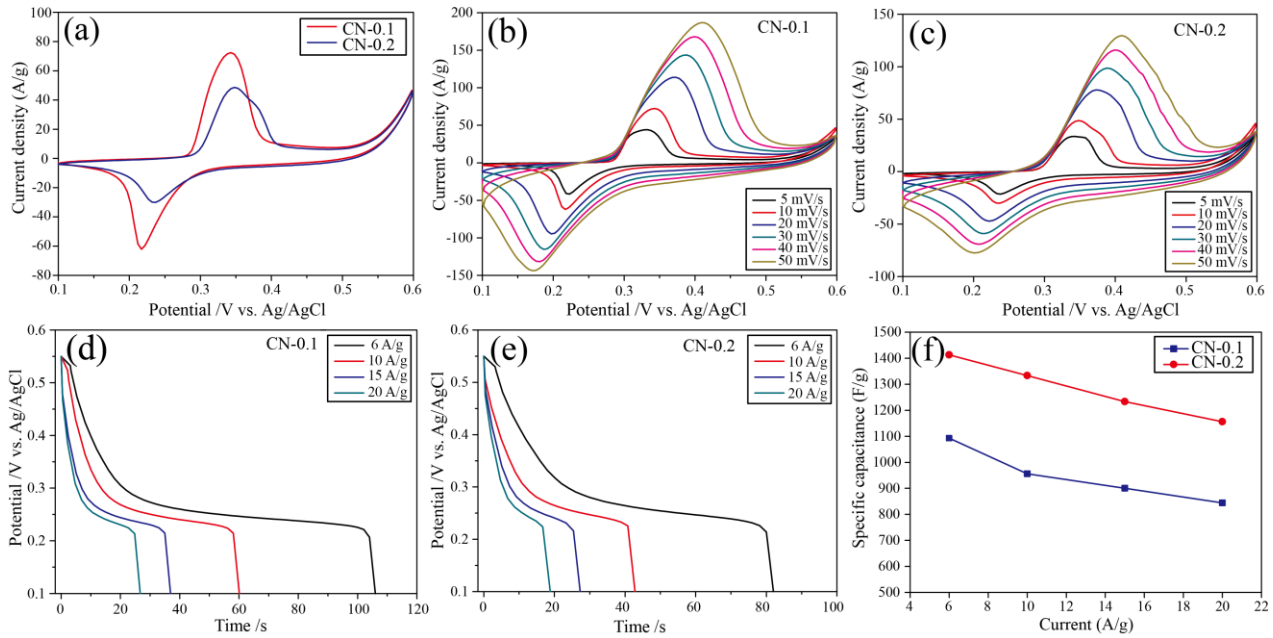


Fig. 4. (a) CV curves of samples CN-0.1 and CN-0.2 at a scan rate of 10 mV/s; (b) and (c) CV curves of samples CN-0.1 and CN-0.2 at scan rates of 5, 10, 20, 30, 40, and 50 mV/s; (d) and (e) galvanostatic discharge curve of samples CN-0.1 and CN-0.2 at current densities of 6, 10, 15, and 20 A/g; (f) specific capacitance of samples CN-0.1 and CN-0.2 at current densities of 6, 10, 15, and 20 A/g.

In order to understand the different levels of retention in the same current-density variation range, EIS analysis is conducted in the frequency range 100 kHz to 0.03 Hz with an alternating current (ac) amplitude of 5 mV. The obtained Nyquist plots are given in Fig. 5(a). The two EIS curves are both composed of a depressed semicircle in high-frequency regions and a straight line in low-frequency regions.²⁸ Obviously, the CN-0.1 electrode exhibits a much smaller semicircle than that of the CN-0.2 electrode, indicating that CN-0.1 has a lower charge-transfer resistance and ion-diffusion resistance with fast reaction kinetics than that of CN-0.2, but both resistance values are much lower than that of pure Ni(OH)₂ [Fig. S5(c)]. Thus it is proved that the Co²⁺ partially substituting for Ni²⁺ in the metal hydroxide enhances the conductivity of Ni(OH)₂, and that specific surface area plays a critical role in its enhancement as well.

Cycling performance of the two electrodes is evaluated by charge-discharge measurements at a

constant current density of 6 A/g in the potential range 0.1–0.45 V for 1000 cycles, as shown in Fig. 5(b). The CN-0.1 electrode shows a 76% capacitance retention, which is higher than that of the CN-0.2 electrode (68%), and both values are higher than that of pure Ni(OH)₂ [47%; see supporting information in Fig. S5(d)]. According to the results, the CN-0.1 electrode has better cycling stability than that of CN-0.2, which may be attributed to the higher specific surface area of sample CN-0.1.

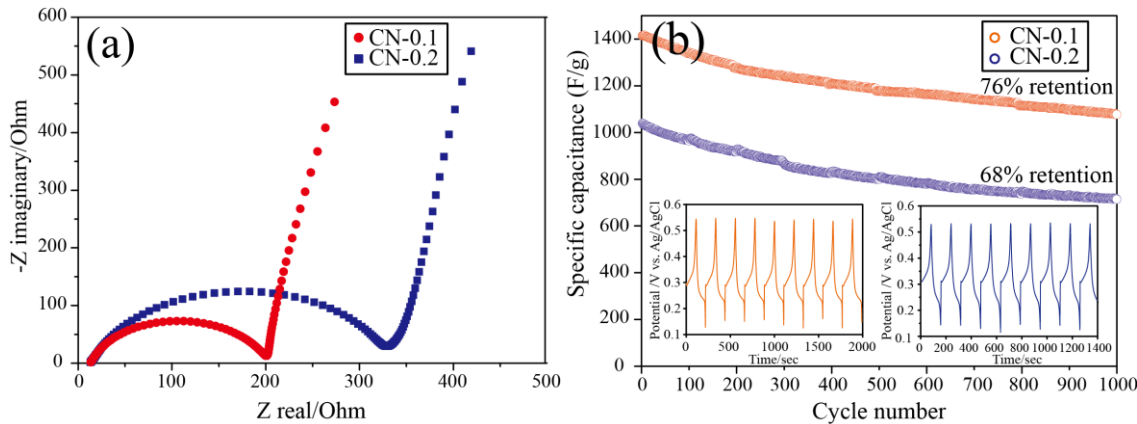


Fig. 5. (a) Nyquist plots of samples CN-0.1 and CN-0.2; (b) cycling performance of samples CN-0.1 and CN-0.2 at a discharge current density of 6 A/g.

In order to evaluate the stability of cobalt-doping performance at high temperature, we select the sample CN-0.1 as a precursor and heat it in air at 350 °C for 2 h. Figure 6 displays the morphology and phase composition of the annealed product. From Figs. 6(a) and 6(b) we can see that the nanosheet network is well inherited from the corresponding precursor after thermal calcination treatment, indicating good structural stability. A high-resolution TEM image [Fig. 6(c)] reveals that the curly nanosheets are composed of numerous ultrafine nanocrystalline particles with a periodic fringe spacing of 0.24 nm. Further, selected-area electron-diffraction (SAED) patterns [inset of Fig. 6(c)] and XRD spectra [Fig. 6(e)] confirm that the Ni(OH)₂ is completely transformed into NiO (JCPDS 04-0835) by calcination. The three marked diffraction rings correspond to the (111), (200), and (220) planes of NiO, respectively. The intensities of the peaks are very weak and broad, implying the small crystal size of the particles. No obvious peaks for cobalt oxides or other impurities are detected in the XRD pattern,

and elemental mapping in Fig. 6(d) shows that Co, Ni, and O are uniformly distributed along the entire nanosheet network; these results together suggest that Co is successfully and homogeneously doped into the lattice of NiO.

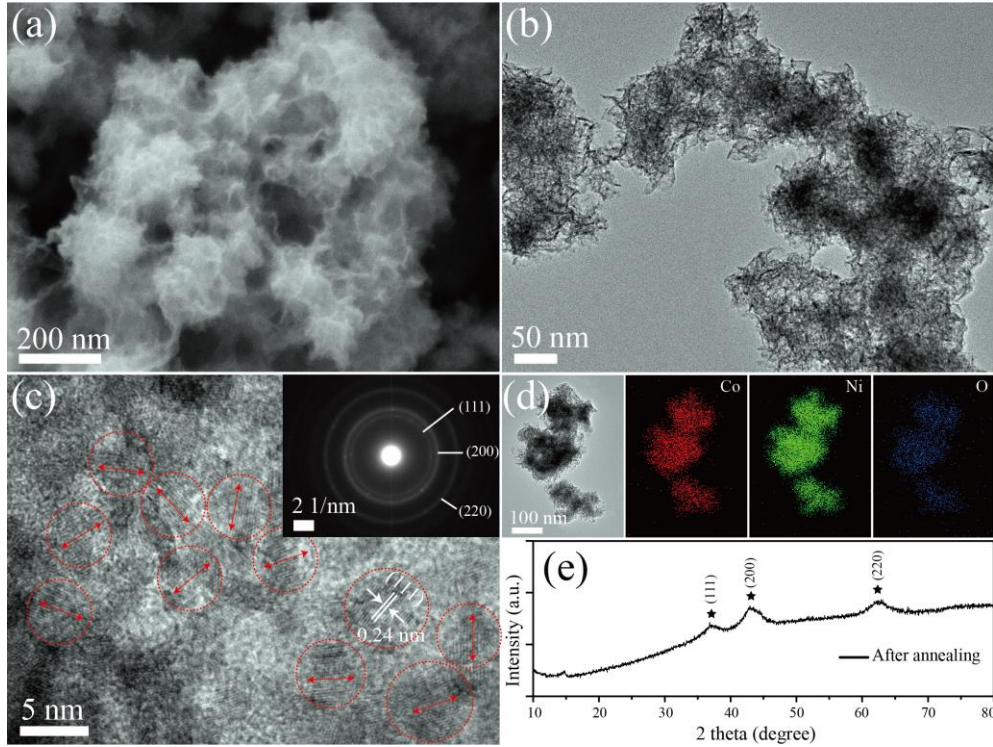


Fig. 6. (a) FESEM image; (b)–(d) TEM images, SAED pattern [inset of panel (c)], and corresponding EDS mapping; (e) XRD spectra of Co-doped NiO.

The electrochemical performance of the Co-doped NiO nanosheet network as an electrode material for a supercapacitor is investigated by cyclic voltammetry, galvanostatic charge-discharge measurements, and EIS analysis in 1 M KOH (Fig. 7). Two strong redox peaks are observed in Fig. 7(a), indicating the pseudocapacitive performance of the supercapacitor,³⁹ and the anodic and cathodic peaks are attributed to the conversion between NiO and NiOOH due to OH⁻ insertion and desorption:



After 1000 continuous charge-discharge cycles, we found that the Co-doped NiO nanosheet network electrode delivers a high specific capacitance of 720 F/g at 6 A/g with 92% retention [Fig.

7(d)], which is superior to that of other reported pure NiO electrodes (Table 1), suggesting its good rate capability and excellent cycling stability.

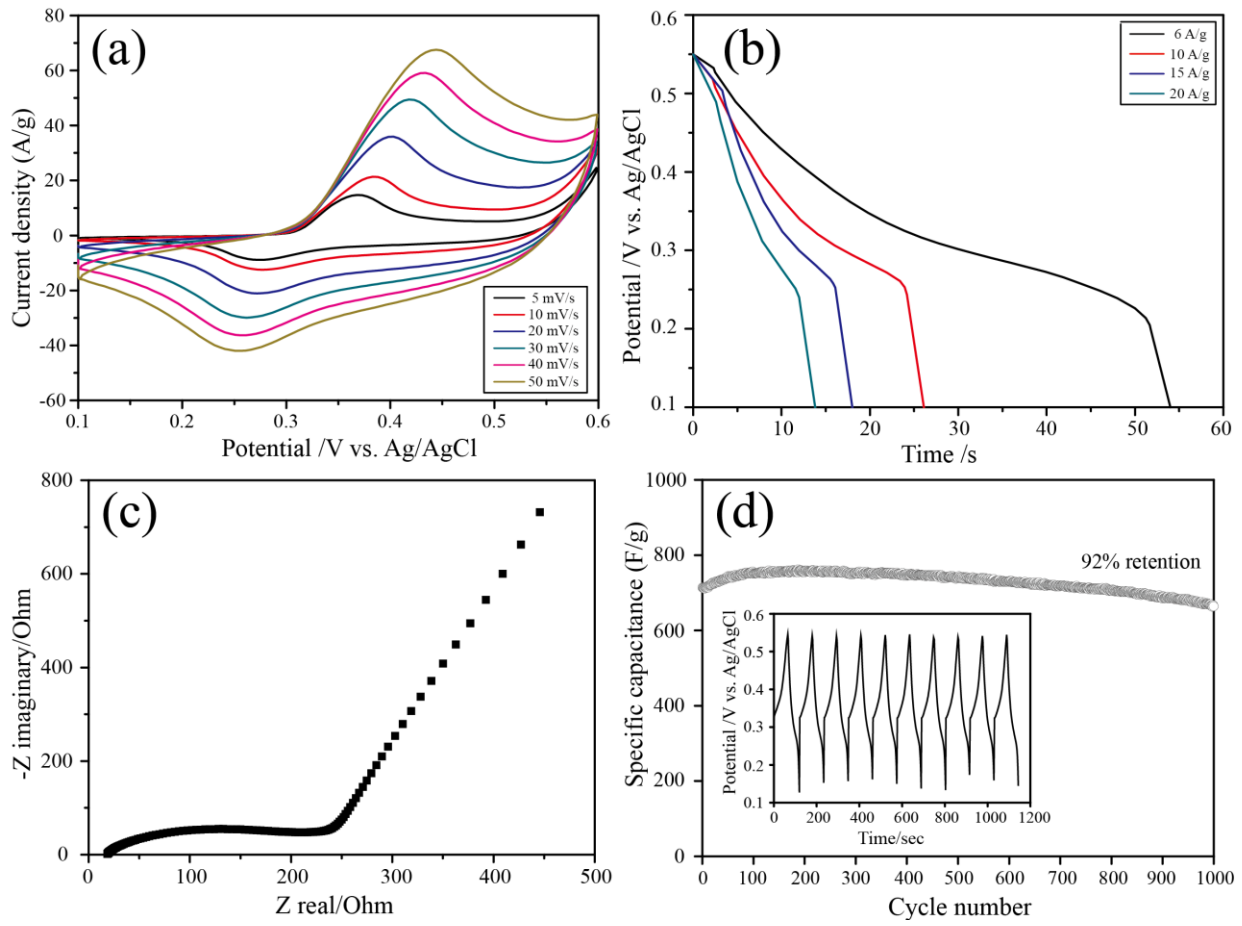


Fig. 7. (a) CV curves of Co-doped NiO at scan rates of 5, 10, 20, 30, 40, and 50 mV/s; (b) galvanostatic discharge curve of Co-doped NiO at current densities of 6, 10, 15, and 20 A/g; (c) Nyquist plots of Co-doped NiO; (d) cycling performance of Co-doped NiO at a discharge current density of 6 A/g.

Overall, the ultrahigh capacitance, excellent rate capability, long cycle life, and low resistance of Co-doped Ni hydroxide and oxide originate from three main factors: (1) The Co^{2+} partially substitutes for Ni^{2+} in the metal hydroxide and oxide, resulting in an increase of free holes in the valence band, therefore enhancing the *p*-type conductivity of Ni(OH)_2 and NiO; (2) the nanosheet network structures with high specific surface area and numerous mesoporosities are able to enlarge the electrode-electrolyte contact area and shorten the path length for ion transport, leading to fast kinetics; (3) it is

reported that some metal oxides or hydroxides will have better reactivity for pseudocapacitor performance when they have a low crystalline or amorphous structure, and this may be another reason for their excellent performance.^{41,43,50}

Table 1 Comparison of various relative results of nickel oxide supercapacitors.

Material	Specific capacitance (F/g)	Current density (A/g)	Electrolyte	Retention	Reference
NiO nanosheet hollow spheres	415	3	2 M KOH	91%	⁵¹
NiO hierarchical nanostructures	425	2	2 M KOH	85%	³⁹
NiO nanoparticle tubes	417	5	2 M NaOH	62%	⁵²
NiO film	250	2	2 M KOH	66%	⁵³
NiO microspheres	455	0.5	5 M KOH	70%	⁵⁴
NiO nanoflower	333	2	2 M KOH	90%	⁵⁵
NiO nanoslices	65	2	2 M KOH	65%	⁵⁵
NiO nanosheet network	720	6	1 M KOH	92%	This work

4. Conclusions

In summary, we report a facile and green process to synthesize a Co-doped Ni(OH)₂ nanosheet network structure combining the LAL technique and aging treatment under room temperature. The morphology and specific surface area of the doped Ni(OH)₂ can be successfully adjusted by changing the concentration of sodium thiosulfate, and it can be easily converted into Co-doped NiO via thermal decomposition in air without changing its pristine morphology. The resulting Co-doped Ni(OH)₂ electrode exhibits an ultrahigh specific capacitance of 1421 F/g at 6 A/g and a good retention level of 76% after 1000 cycles in 1 M KOH aqueous solution, and the Co-doped NiO electrode exhibits a capacitance of 720 F/g and 92% retention under the same conditions. The performance of both pseudocapacitors is dramatically improved compared to that of undoped components. Electrochemical tests demonstrate that Co-doping and morphology control strategies can effectively improve

pseudocapacitor performance of nickel hydroxide and oxide. The enhanced pseudocapacitor performance can be attributed to the synergistic effect contribution from improved electronic conductivity, low crystalline structure, higher specific surface area, and more mesoporosities, which will enlarge the electrode-electrolyte contact area and shorten the path length for ion transport. This work provides an innovative approach for fabricating Co-doped Ni(OH)₂ nanomaterials; more significantly, it is instructive for construction of other mesoporous and doped metal oxides and hydroxides for broader applications, such as electrocatalytic water oxidation, active layers for hybrid solar cells, and electrode materials for lithium ion batteries.

Acknowledgments

This work was supported by the National Basic Research Program of China (2014CB931704), the National Natural Science Foundation of China (NSFC, no. 11174287, 51371166, 11204308).

Electronic Supplementary Information (ESI) available: [Preparation and characterization of pure Ni(OH)₂ nanosheets, additional EDX, TEM analysis of sample CN-0.1, CN-0.2, CV and EIS test of pure Ni(OH)₂ nanosheet networks, Nyquist plots of sample CN-0.2]. See DOI: 10.1039/x0xx00000x

References

- [1] M. Li, Z. Tang, J. M. Xue, *Adv. Funct. Mater.*, 2014, **24**, 7495–7502.
- [2] J. Zhi, W. Zhao, F. Q. Huang, *Adv. Funct. Mater.*, 2014, **24**, 2013–2019.
- [3] J. Yang, C. Yu, X. M. Fan, C. T. Zhao, J. S. Qiu, *Adv. Funct. Mater.*, 2015, **25**, 2109–2116.
- [4] C. Yu, J. Yang, C. T. Zhao, X. M. Fan, J. S. Qiu, *Nanoscale*, 2014, **6**, 3097–3104.
- [5] J. Yang, C. Yu, X. M. Fan, J. S. Qiu, *Adv. Energy Mater.*, 2014, **4**.
- [6] Y. Q. Zhu, C. B. Cao, W. S. Chu, Y. D. Li, *Scientific Reports*, 2014, **4**, 5787.
- [7] R. T. Wang, J. W. Lang, X. B. Yan, *NPG Asia Materials*, 2015, **7**, e183.
- [8] H. M. Du, L. F. Jiao, H. T. Yuan, *ACS Appl. Mater. Interfaces*, 2013, **5**, 6643–6648.

- [9] J. T. Li, W. Zhao, N. Q. Wu, *Nanoscale*, 2011, **3**, 5103–5109.
- [10] X. Q. Tian, C. M. Cheng, D. Xiao, *J. Mater. Chem.*, 2012, **22**, 8029–8035.
- [11] J. X. Li, M. Yang, Z. Zhou, *Nanoscale*, 2012, **4**, 4498–4503.
- [12] X. W. Li, S. L. Xiong, Y. T. Qian, *J. Mater. Chem.*, 2012, **22**, 14276–14283.
- [13] J. C. Huang, T. Lei, X. P. Wei, *Journal of Power Sources*, 2013, **232**, 370–375.
- [14] R. Oesten, M. Kasper, R. A. Huggins, *Ionics*, 1996, **2**, 293–301.
- [15] C. C. Miao, Y. J. Zhu, T. Q. Zhao, *Journal of Power Sources*, 2015, **274**, 186–193.
- [16] G. Lee, C. V. Varanasi, J. Liu, *Nanoscale*, 2015, **7**, 3181–3188.
- [17] X. Chen, C. L. Long, Z. J. Fan, *Electrochimica Acta*, 2014, **137**, 352–358.
- [18] G. Anandha babu, G. Ravi, Y. Hayakawa, *J. Phys. Chem. C*, 2014, **118**, 23335–23348.
- [19] J. Y. Ma, L. W. Yin, T. R. Ge, *CrystEngComm*, 2015, **17**, 9336–9347.
- [20] J. H. Zhang, G. F. Cai, C. D. Gu, J. P. Tu, *J. Mater. Chem. C*, 2014, **2**, 7013–7021.
- [21] Y. J. Mai, J. P. Tu, X. H. Xia, C. D. Gu, *Journal of Power Sources*, 2011, **196**, 6388–6393.
- [22] T. V. Thi, A. K. Rai, J. Kim, *Journal of Power Sources*, 2015, **292**, 23–30.
- [23] H. M. Zhang, C. H. Liang, *J. Phys. Chem. C*, 2010, **114**, 12524–12528.
- [24] X. Y. Liu, Y. Q. Gao, G. W. Yang, *Nanoscale*, 2016, **8**, 4227–4235.
- [25] Z. F. Tian, C. H. Liang, L. D. Zhang, *J. Mater. Chem.*, 2011, **21**, 18242–18247.
- [26] D. W. Liang, Z. F. Tian, C. H. Liang, *Electrochimica Acta*, 2015, **182**, 376–382.
- [27] J. W. Nai, Y. Tian, L. Guo, *J. Am. Chem. Soc.*, 2013, **135**, 16082–16091.
- [28] C. Long, M. T. Zheng, Y. L. Liu, *ACS Appl. Mater. Interfaces*, 2015, **7**, 24419–24429.
- [29] Z. F. Tian, Y. X. Ye, C. H. Liang, *CrystEngComm*, 2015, **17**, 3015–3022.
- [30] H. M. Zhang, Z. F. Tian, C. H. Liang, *Phys. Chem. Chem. Phys.*, 2013, **15**, 5684–5690.
- [31] Y. J. Zhang, Y. M. Leng, *Dalton Trans.*, 2013, **42**, 5485–5490.
- [32] J. W. Nai, H. J. Yin, Z. Y. Tang, L. Guo, *Adv. Energy Mater.*, 2015, **5**, 1401880.
- [33] J. W. Nai, S. Q. Wang, L. Guo, *Small*, 2013, **18**, 3147–3152.

- [34] J. W. Lee, J. M. Ko, J. D. Kim, *J. Phys. Chem. C*, 2011, **115**, 19445–19454.
- [35] D. H. Sun, J. L. Zhang, D. X. Sun, *J. Phys. Chem. C*, 2010, **114**, 12110–12116.
- [36] S. D. Min, C. J. Zhao, Z. M. Zhang, Z. P. Guo, *J. Mater. Chem. A*, 2015, **3**, 3641–3650.
- [37] Z. W. Zhang, L. W. Yin, *J. Mater. Chem., A* 2015, **3**, 17659–17668.
- [38] H. Chen, L. F. Hu, M. Chen, *Adv. Funct. Mater.*, 2014, **24**, 934–942.
- [39] J. Min, M. Lei, W. J. Wang, N. Su, *ACS Appl. Mater. Interfaces*, 2016, **8**, 780–791.
- [40] X. H. Liu, R. Z. Ma, Y. Bando, T. Sasaki, *Adv. Funct. Mater.*, 2014, **24**, 4292–4302.
- [41] H. B. Li, M. H. Yu, F. X. Wang, G. W. Yang, *Nature Communications*, 2013, **4**, 1894.
- [42] J. L. Bantignies, S. Deabate, F. Henn, *J. Phys. Chem. C*, 2008, **112**, 2193–2201.
- [43] H. B. Li, H. M. Yu, P. Lu, *ACS Appl. Mater. Interfaces*, 2014, **6**, 745–749.
- [44] G. X. Zhu, Y. J. Liu, X. P. Shen, *CrystEngComm*, 2013, **15**, 9189–9195.
- [45] L. Wang, Z.H. Dong, Z. G. Wang, J. Jin, *Adv. Funct. Mater.*, 2013, **23**, 2758–2764.
- [46] J. W. Lee, J. M. Ko, J. D. Kim, *J. Phys. Chem. C*, 2011, **115**, 19445–19454.
- [47] D. P. Dubal, G. S. Gund, R. Holze, *ACS Appl. Mater. Interfaces*, 2013, **5**, 2446–2454.
- [48] L. J. Li, J. Xu, J. L. Lei, Z. D. Wei, *J. Mater. Chem. A*, 2015, **3**, 1953–1960.
- [49] C. Z. Yuan, J. Y. Li, S. L. Xiong, *J. Mater. Chem. A*, 2013, **1**, 11145–11151.
- [50] Y. Fu, J. M. Song, Y. Q. Zhu, C. B. Cao, *Journal of Power Sources*, 2014, **262**, 344–348.
- [51] S. J. Ding, T. Zhu, J. S. Chen, X. W. Lou, *J. Mater. Chem.*, 2011, **21**, 6602–6606.
- [52] Q. Li, C. L. Liang, X. F. Lu, G. R. Li, *J. Mater. Chem. A*, 2015, **3**, 6432–6439.
- [53] M. L. Huang, C. D. Gu, X. Ge, J. P. Tu, *Journal of Power Sources*, 2014, **259**, 98–105.
- [54] D. D. Han, P. C. Xu, X. Y. Jing, M. L. Zhang, *Journal of Power Sources*, 2013, **235**, 45–53.
- [55] S. I. Kim, J. S. Lee, H. K. Song, J. H. Jang, *ACS Appl. Mater. Interfaces*, 2013, **5**, 1596–1603.